

# Revealing Hidden Variability in PWNe With Spectral Index Maps

Benson T. Guest,<sup>1,2,3,4</sup>★ Samar Safi-Harb,<sup>1</sup>†

<sup>1</sup>*Department of Physics and Astronomy, University of Manitoba, 30a Sifton Rd, Winnipeg R3T 2N2, Canada*

<sup>2</sup>*Department of Astronomy, University of Maryland, College Park, MD 20742, USA*

<sup>3</sup>*X-ray Astrophysics Laboratory, NASA/GSFC, Greenbelt, MD 20771, USA*

<sup>4</sup>*Center for Research and Exploration in Space Science and Technology, NASA/GSFC, Greenbelt, MD 20771, USA*

Accepted XXX. Received YYY; in original form ZZZ

## ABSTRACT

Pulsar wind nebulae (PWNe) are the synchrotron bubbles inflated by the rotational energy of a neutron star. Observing variability within them has previously been limited to cases of significant brightening, or the few instances where transient features are interpreted in terms of intrinsic motion or associated with variability from the pulsar. Jet and torus morphology are also only visible in cases of differing brightness with respect to the surrounding nebula and favourable alignment with our line of sight. Spectral map analysis involves binning observations with an adaptive algorithm to meet a signal limit and colouring the results based on the desired model parameter fits. Minute changes in spectral index become therefore apparent even in cases where brightness images alone do not suggest any underlying changes. We present a *Chandra* X-ray study of the PWNe in G21.5–0.9, Kes 75, G54.1+0.3, G11.2–0.3, and 3C 58, using archival observations accumulated over the ~20-year lifetime of the mission. With the spectral map analysis technique, we discover evidence for previously unknown variability opening a new window into viewing PWNe.

**Key words:** ISM: supernova remnants, ISM: individual: G21.5–0.9, Kes 75, G54.1+0.3, G11.2–0.3, 3C 58

## 1 INTRODUCTION

Pulsar wind nebulae (PWNe) are the synchrotron bubbles inflated by the rotational energy of a neutron star (or pulsar). Their study sheds light on their powering engine and the interaction of the relativistic pulsar’s wind with its surrounding supernova remnant ejecta or the ISM. The theory of pulsar winds for many years was assumed to closely follow the work of Kennel & Coroniti (1984a,b) who derived a spherically symmetric MHD model for the evolution, and emission profile for a PWN with synchrotron losses. High resolution X-ray observations have shown that the spectral index ( $\alpha$ ,  $S_\nu \sim \nu^{-\alpha}$ ) in resolved PWNe does not increase as rapidly as predicted by the spherically symmetric model (see e.g., Guest et al. (2019) and references therein). Alternative models have been proposed such as diffusion (Tang & Chevalier 2012), extending the MHD analysis to 3-D (Del Zanna et al. 2018), or a combination of both (Porth et al. 2016). Spectral maps trace the distribution of particles in both en-

ergy and position, and X-ray emitting electrons trace the freshly injected high-energy particles suffering higher synchrotron losses. Comparison of observed and simulated spectral maps allows an understanding and testing of pulsar wind propagation models.

Observing variability within pulsar wind nebulae has previously been limited to cases of significant brightening, or the few instances where transient features are interpreted in terms of intrinsic motion (Pavlov et al. 2001; Hester et al. 2002; DeLaney et al. 2006) or associated with an occasional magnetar-like outburst from the pulsar (Blumer et al. 2017; Younes et al. 2016; Kumar & Safi-Harb 2008; Ng et al. 2008). In particular, jet and torus morphology have been only visible in cases of differing brightness with respect to the surrounding nebula and favourable alignment with our line of sight. Spectral map analysis involves binning observations with an adaptive algorithm to meet a signal to noise ratio limit and colouring the results based on the desired model parameter fits. Changes in spectral index can become apparent in areas which do not stand out in brightness images alone. In this work, we show that this technique reveals evidence of previously hidden structures and changes

★ E-mail: umguest@myumanitoba.ca

† E-mail: samar.safi-harb@umanitoba.ca

in the emitting particle spectrum where traditional RGB and brightness images have provided little insight.

## 2 OBSERVATIONS AND METHODS

In this work, we focus on archival *Chandra* X-ray observations of relatively young and bright PWNe which have been observed multiple times over the lifetime of the mission. In Table 1 we summarize our targets (G21.5–0.9, Kes 75, G11.2–0.3, G54.1+0.3 and 3C 58) and the corresponding observations taken with *Chandra* between its launch in 1999 and the latest observation acquired at the time of this work. We selected these objects given their relative youth and brightness, their dominant non-thermal synchrotron X-ray emission from the PWN, as well as the frequency of archived *Chandra* observations. We note that given their small size, *Chandra* is the most adequate and powerful satellite that allows such a detailed study. All observations reported are acquired using the Advanced CCD Imaging Spectrometer (ACIS). Data processing was performed using the Chandra Interactive Analysis of Observations (CIAO) software package (Fruscione et al. 2006), while spectral analysis made use of the X-ray spectral fitting package XSPEC version 12.9.1 (Arnaud 1996).

### 2.1 The Sample

#### 2.1.1 G21.5–0.9

G21.5–0.9 (Figure 1 (1)) is a plerionic composite supernova remnant (SNR) located at a distance of 4.8 kpc (Tian & Leahy 2008). The bright PWN has been used as a calibration target for X-ray missions and has been observed regularly over the 20-year lifetime of the *Chandra* X-ray Observatory. The PWN has a circular morphology extending out to a radius of  $\sim 40''$  with steepening spectral index with distance from the centre, and is surrounded by a very faint limb-brightened shell which radiates primarily non-thermal emission (Slane et al. 2000; Safi-Harb et al. 2001; Matheson & Safi-Harb 2005). The only significant source of thermal emission is found from a small knot to the north (Guest et al. 2019; Matheson & Safi-Harb 2010; Bocchino et al. 2005; Matheson & Safi-Harb 2005). The PWN is powered by the 62 ms pulsar discovered independently in the radio by Gupta et al. (2005) and Camilo et al. (2006). Bietenholz & Bartel (2008) measured a PWN expansion age of  $870^{+200}_{-150}$  years using Very Large Array (VLA) observations from 1991 and 2006 making G21.5–0.9 one of the youngest known Galactic PWNe.

#### 2.1.2 Kes 75

Kes 75 (Figure 1 (2)) is a plerionic composite SNR at a distance of 5.8 kpc (Verbiest et al. 2012). The PWN measures  $\sim 26'' \times 20''$  with thermal emission from the supernova remnant shell seen in clumps to the south (Helfand et al. 2003). The PWN displays inner structure including a jet directed to the south (Morton et al. 2007). The 324 ms pulsar (Gotthelf et al. 2000) emitted several magnetar-like outbursts from 2000–2006 (Gavril et al. 2008; Kumar & Safi-Harb 2008). This resulted in a softening of the spectrum of the pulsar and

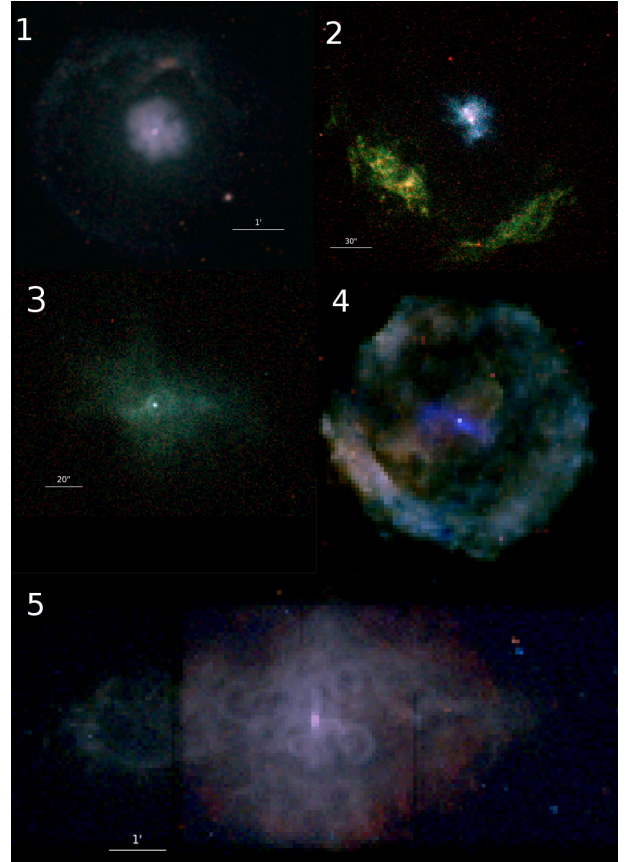


**Figure 1.** Images of the SNRs observed: (1) G21.5–0.9, (2) Kes 75, (3) G54.1+0.3, (4) G11.2–0.3, and (5) 3C 58. The RGB images are coloured using the energy ranges 0.5–1.2 keV, 1.2–2 keV, and 2–7 keV for red, green, and blue, respectively.

a brightening of the southern jet from 2000 to 2006 (Kumar & Safi-Harb 2008; Ng et al. 2008). Reynolds et al. (2018) found a PWN expansion age of  $400 \pm 40$  yr making Kes 75 the youngest known Galactic PWN.

#### 2.1.3 G54.1+0.3

G54.1+0.3 (Figure 1 (3)) is a plerionic SNR at an estimated distance of 6.3 kpc (Shan et al. 2018). The SNR displays a bright point source, surrounding ring, and jet-like elongations to the east and west (Lu et al. 2002). While the X-ray emission is all non-thermal, an infrared shell was found by (Temim et al. 2010) who interpreted the emission as ejecta dust heated by early type stars within the expanding SNR. The 137 ms pulsar powering the nebula was discovered in the radio band by (Camilo et al. 2002), who calculated a characteristic age of 2900 years.

#### 2.1.4 G11.2–0.3

G11.2–0.3 (Figure 1 (4)) is a plerionic composite SNR (Vasisht et al. 1996) located at a distance of 5.5–7 kpc (Minter et al. 2008). The PWN is powered by a 65 ms pulsar discovered by (Torii et al. 1997) using *ASCA* X-ray observations. The PWN is elongated with jet-like morphology and broadening at the centre consistent with a torus viewed edge-on

(Kaspi et al. 2001; Roberts et al. 2003). The SNR shell displays a circular morphology. Borkowski et al. (2016) measured expansion of the shell from 2000–2013. Free expansion places an upper limit of the age as 3600 years however, they argue due to the advanced dynamical age where nearly all the ejecta have been shocked, significant deceleration must have occurred. The unknown density distribution of the surrounding medium leads to age estimates of 1400–2400 years.

### 2.1.5 3C 58

3C 58 (Figure 1 (5)) is a Crab-like SNR possibly associated with the historical supernova event of 1181 C.E. (Stephenson 1971) and located at a distance of 2 kpc (Kothes 2013, 2016). The 66 ms pulsar was discovered by (Murray et al. 2002). The PWN displays a central jet and torus morphology surrounding the pulsar, the nebula is full of loops and twists, while the outer PWN is embedded in thermal X-ray emission enriched with Ne and Mg suggesting its origin as swept-up ejecta (Slane et al. 2004; Gotthelf et al. 2007).

## 2.2 Methods

Typically, regions of interest are selected based on the appearance of a brightness or RGB colour image. Here we use the adaptive binning software *CONTBIN* (Sanders 2006) to generate regions following the surface brightness of an input image and meeting a specified signal limit. This limit may be a signal to noise value calculated using a background region, or simply a minimum number of counts. For our analysis where background contribution is relatively small and expected to be uniform across the individual nebulae we use minimum number of counts. This creates puzzle-like pieces that fit together completely covering the area of interest while leaving no gaps and allowing a study of features which may not have been selected for targeted study using handmade regions or that may have been inadvertently averaged over using different region construction methods. Spectra are then extracted from each region and a background taken from outside the PWN, binned to a minimum of 10 counts per bin and fit with the X-ray spectral fitting software *XSPEC* (Arnaud 1996). We assume that the column density (TBABS model in XSPEC with abundances provided by Wilms et al. (2000)) does not vary over the size of the nebula and freeze this parameter to the best fit value derived from the PWN spectrum. The regions are then coloured according to the values of the desired model parameter to generate maps. When the emission is not purely non-thermal (such as in 3C 58) we can identify the regions where a single component model is insufficient through the construction of a reduced chi-square map and add the thermal component where necessary. Additionally, in cases where there is significant contribution to the surface brightness from the thermal emission associated with the SNR (such as in G11.2–0.3) we restrict our input image and fitting range to the hard X-ray band from 3.5 – 8 keV where the non-thermal synchrotron emission from the PWN is dominant.

Pileup occurs when multiple photons are received within the readout time of the detector. These are indistinguishable from a single photon with the sum of the energy. Of our sources, Kes 75, G11.2–0.3 and G54.1+0.3 each has

**Table 1.** Observation ID, date, ACIS chip ID and exposure time of the *Chandra* observations used. Data were collected from the Chandra Data Archive (<https://cda.harvard.edu/chaser/>).

| Obs ID           | Date of Obs | ACIS Chip | Exp Time (ks) |
|------------------|-------------|-----------|---------------|
| <b>G21.5–0.9</b> |             |           |               |
| 1433             | 1999-11-15  | S3        | 14.97         |
| 1717             | 2000-05-23  | S3        | 7.54          |
| 1725             | 2000-05-24  | I3        | 7.57          |
| 1726             | 2000-05-24  | I3        | 7.57          |
| 1838             | 2000-09-02  | S3        | 7.85          |
| 1839             | 2000-09-02  | S3        | 7.66          |
| 2872             | 2002-09-13  | I3        | 9.84          |
| 2873             | 2002-09-14  | S3        | 9.83          |
| 3699             | 2003-11-09  | I3        | 9.7           |
| 4353             | 2003-05-15  | S3        | 9.36          |
| 5158             | 2005-02-26  | I3        | 10            |
| 5165             | 2004-03-26  | I3        | 9.55          |
| 5166             | 2004-03-14  | S3        | 10.02         |
| 6070             | 2005-02-26  | I3        | 9.43          |
| 6071             | 2005-02-26  | S3        | 9.64          |
| 6740             | 2006-02-21  | I3        | 9.83          |
| 6741             | 2006-02-22  | S3        | 9.83          |
| 8371             | 2007-05-28  | I3        | 9.92          |
| 10644            | 2009-05-29  | S2        | 9.64          |
| 10645            | 2009-05-29  | S2        | 9.54          |
| 10646            | 2009-05-29  | S3        | 9.54          |
| 14263            | 2012-08-08  | S3        | 9.57          |
| 14264            | 2012-08-10  | I3        | 9.57          |
| 16420            | 2014-05-07  | S3        | 9.57          |
| 16421            | 2014-05-09  | I3        | 9.57          |
| <b>Kes 75</b>    |             |           |               |
| 748              | 2000-10-15  | I2        | 37.28         |
| 57337            | 2006-06-05  | S3        | 17.37         |
| 6686             | 2006-06-07  | S3        | 54.1          |
| 7338             | 2006-06-09  | S3        | 39.25         |
| 7339             | 2006-06-12  | S3        | 44.11         |
| 10938            | 2009-08-10  | S3        | 44.61         |
| 18030            | 2016-06-08  | S3        | 84.95         |
| 18866            | 2016-06-11  | S3        | 61.46         |
| <b>G11.2–0.3</b> |             |           |               |
| 780              | 2000-08-06  | I2        | 19.74         |
| 781              | 2000-10-15  | I2        | 9.97          |
| 2322             | 2000-10-15  | I2        | 4.85          |
| 3909             | 2003-05-10  | I2        | 13.78         |
| 3910             | 2003-06-27  | I2        | 13.78         |
| 3911             | 2003-08-01  | S0        | 14.6          |
| 3912             | 2003-09-08  | I2        | 14.68         |
| 14831            | 2013-05-05  | S3        | 173.02        |
| 14830            | 2013-05-25  | S3        | 58.24         |
| 14832            | 2013-05-26  | S3        | 63.23         |
| 15652            | 2013-09-07  | S3        | 47.93         |
| 16323            | 2013-09-08  | S3        | 45.76         |
| <b>G54.1+0.3</b> |             |           |               |
| 1983             | 2001-06-06  | I2        | 38.46         |
| 9886             | 2008-07-08  | I2        | 65.33         |
| 9108             | 2008-07-10  | I2        | 34.67         |
| 9109             | 2008-07-12  | I2        | 162.25        |
| 9887             | 2008-07-15  | I2        | 24.84         |
| <b>3C 58</b>     |             |           |               |
| 728              | 2000-09-04  | S3        | 49.95         |
| 3832             | 2003-04-26  | S3        | 135.83        |
| 4382             | 2003-04-23  | S3        | 167.39        |
| 4383             | 2003-04-22  | S3        | 38.73         |

a pulsar which suffers from pile-up. Methods of correcting for pileup require extracting spectra from a region covering the entire point spread function in order to correct for the effect. Our bins surrounding the point source do not meet this requirement, we therefore leave analysis of the central region to traditional methods and other studies, and focus instead on the extended nebular emission which is not piled up.

We investigate changes by creating a merged image to use as the input for region creation. We choose to use a merged image as input to avoid biasing our results towards a single observation. We choose a minimum counts limit such that even the shortest observation will yield a few hundred counts in each region while also attempting to conserve as much inherent structure through keeping the regions as small as possible. Background was taken from regions outside of the remnant while remaining on the same ACIS chip. In each case the background scaled to the individual region sizes is expected to contribute minimally ( $\lesssim 5$  counts) to the overall total. This combined with our limit of at least  $\sim 300$  counts per spectrum allows for the use of chi-squared statistics. Spectra were extracted from the same set of regions for each observation, and those from a common year were fit simultaneously allowing a direct comparison. Significant changes were identified through creating error maps using the same process as above. Regions are coloured according to the significance of the difference. This was calculated using the following expression:  $(\Gamma_1 - \Gamma_2) / \sqrt{\sigma_1^2 + \sigma_2^2}$ , where  $\Gamma$  is the best-fit photon index for each observation period, and  $\sigma$  is the 1-sigma error value associated with each fit. Differences are deemed significant if they exceed the 2-sigma level.

Our analysis introduces several choices which may affect the results. One obvious choice is the signal limit parameter within *Contbin* which alters the number of counts required per region, and therefore defines the resulting region size. The variability we see appears to happen on the scale of a few arcseconds. Increasing the region size much above this has the effect of smoothing out any variability. When we increase the region size sufficiently we no longer see variability and we return to the previous result of PWNe being remarkably stable on large scales. Optimising the region size to produce the best statistics while retaining evidence of variability is complicated by the entanglement of the typical brightness profile of young PWNe and the *Contbin* algorithm. PWNe are brightest in the centre close to the pulsar and decrease in brightness to the edge of the nebula. As a result *Contbin* generates smaller regions close to the pulsar with regions growing larger with distance. In order to examine the effect of region size and statistics we extract spectra from circles of increasing size centred on the region to the north of the pulsar in G21.5-0.9 which showed significant hardening between 2000 and 2005 (Figure 3). For each circle size we compare the difference in photon index and its significance between the 2000 and 2005 observations. We find the significance increases to a maximum for a radius of  $3''$  and then decreases for larger radii. This roughly matches the size of the *Contbin* region and the number of spectral counts ( $\sim 450$ ) per observation. A second choice is the freezing of the column density parameter across the nebula.

While we do not expect the column density to vary sig-

nificantly over the few tens of arcseconds scale of the remnants we studied, we examine the effect of freeing this parameter in our fits of Kes 75. When we look for significant changes between the 2006 and 2016 observations we lose the significant changes in the southern jet, however the region to the north of the pulsar remains as a region of significant softening. 3C58 is an exception as this remnant spans more than 6 arcminutes along its major axis. We note however that the variability we observe occurs in regions near the pulsar spanning  $\sim 1'$ . A final choice is our threshold for significance. For the number of regions per remnant we have used, it is reasonable to find one or two regions where the observed changes exceed the  $2\sigma$  level by chance coincidence. Our analysis relies on the comparison of two or more observation periods. To constrain the errors to a sufficient level to make a meaningful comparison, both observations need to be of sufficient length and quality. While we use the term significant to describe changes detected at a  $2\sigma$  level, it should be understood that these changes will need to be confirmed with future pairs of deep observations in order to meet the standard  $3\sigma$  detection level.

## 2.3 Analysis

### 2.3.1 G21.5-0.9

We group observations by year to create individual maps and look for variability in the photon index. Figure 2 shows the spectral maps by year of observation. Figures A1 and A2 show the associated photon index errors and reduced chi-squared values. The region of hard photon index to the north of the pulsar found in the combined map of Guest et al. (2019) is not visible in the 1999 observation. It appears hardest in February 2005, and seems to show variability at least on the order of the observation intervals (Table 1); then hardening again in 2007 and 2012 and softening by the final 2014 observation. To check if these changes are statistically meaningful, we create significance images. Figure 3 shows the differences between the 2005 observations where the plume spectrum is the hardest and the 2000 observations. The plume is clearly visible as a region of significant hardening while there is also a region to the south in line with a counter jet that has softened. Figure 4 shows the significant differences over year timescales.

A comparison with brightness variability is shown in Figure 5. Exposure corrected flux images in the broad band (0.5-7 keV) were generated with the *CIAO* scripts *fluximage* for years with a single observation and *merge\_obs* for multiple observation years. The flux images were then binned to match the spectral map regions. The plume to the north of the pulsar shows variability which does not correlate exactly with the changes in photon index. The plume appears brightest in 2006 and 2007 yet is fainter in 2005.

### 2.3.2 Kes 75

To measure the column density, spectra were extracted from a 35 arcsecond radius centred on the pulsar, with a  $5''$  radius circle excluded to avoid pileup. The spectra were then fit simultaneously with an absorbed power-law with a single column density while allowing the photon index and power-law normalizations to vary between the observation years.



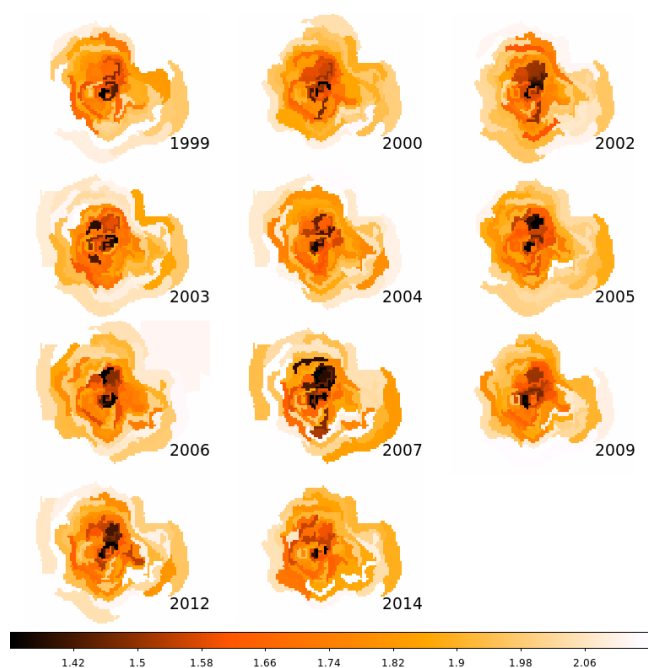


**Figure 2.** Photon index map of G21.5–0.9. The plume of hard emission to the north of the pulsar does not appear in the first year of observations and becomes more noticeable with time, reaching its hardest spectrum in the February 2005 observations. The plume size appears to change as the surrounding regions also show variability. The maximum size is found in the 2007 observation, however we note the increased uncertainties associated with this observation (Figure A1) compared to the other years.

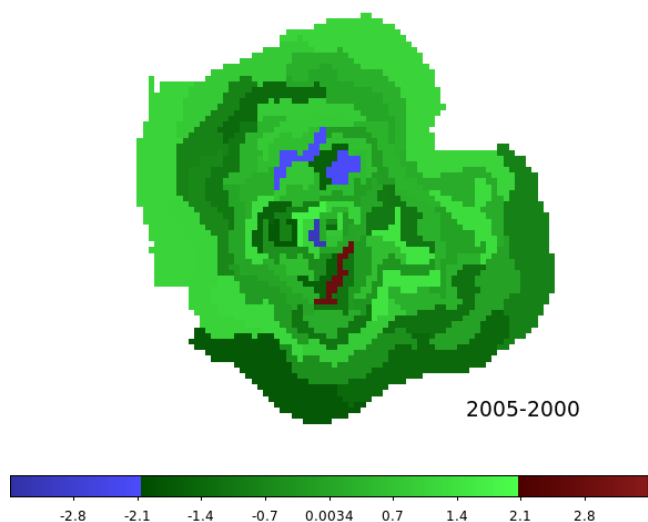


**Figure 3.** G21.5–0.9 significance map showing the changes in photon index between observations taken in 2005 and earlier observations from 2000.

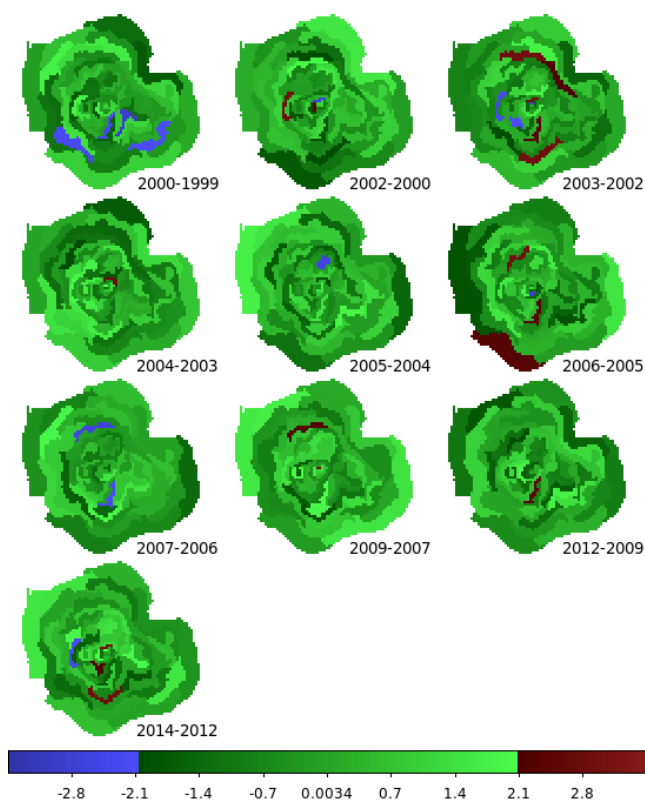


**Figure 4.** Significance map of G21.5–0.9 showing the changes in photon index on year-timescales.

The singular column density value found from this fitting was then held constant for each individual region fit in the subsequent spectral maps.

Figure 6 shows the evolution of the Kes 75 spectral maps. Figures A3 and A4 show the associated photon index error and the reduced chi-squared values. Figure A5 shows the exposure corrected flux maps. The southern jet is observed to have the hardest spectrum along with a counter jet in the 2006 observations. In agreement with (Ng et al. 2008) the hardest region of the jet does not occur closest to the pulsar, rather there is a gap which shows a softer spectral index which is symmetric around the pulsar. The PWN was observed 4 times for 155 ks over a few days in 2006 and twice for 146 ks in 2016. These observations when fit simultaneously offer tighter constraints than the single observations in 2000 and 2009. We therefore look for significant changes between the 2006 and 2016 observations. Figure 7 shows the significance map. There is significant softening in the jet and in a region in the direction of the counter jet, while the rest of the PWN remains largely unchanged. We find hardening between 2006 and 2009 followed by softening between 2009 and 2016 in matching regions. We note the larger errors associated with the 2009 observation (Figure A3) compared to the deep observations of 2006 and 2016.

We look for changes in the greater nebula through the radial spectral analysis shown in Figure 8. Spectra were extracted from rings centred on the pulsar and fit with an absorbed power-law. The central region has been corrected for pile-up. The softening of the pulsar spectrum is observed post outburst in 2006 in agreement with the previous

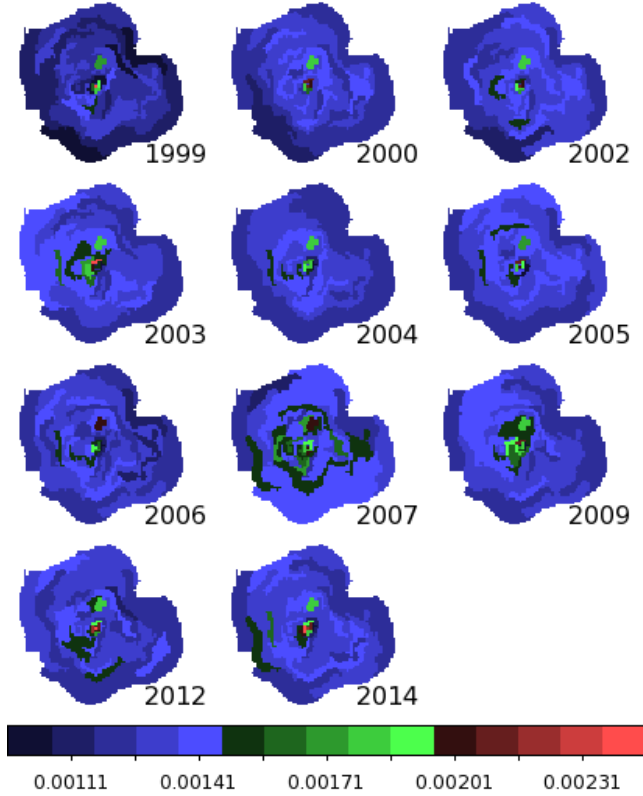


**Figure 5.** Exposure corrected flux maps of G21.5-0.9 (in units of photons  $\text{cm}^{-2}\text{s}^{-1}$ ).

study of Kumar & Safi-Harb (2008), and returns to the pre-outburst levels by 2009. Despite the significant changes seen in the spectral maps, the radial profiles do not reveal similar variations between observations in the nebula.

### 2.3.3 G54.1+0.3

The interesting morphology of G54.1+0.3 with resolved torus and clumpy jets provide an ideal target for spectral map analysis. We see evidence of softening of the torus, most notably on the eastern side and the western jet (Figure 9). Unfortunately, the short observation from 2001 does not allow us to constrain the indices to the degree required to determine if significant changes have occurred (Figures A6 and 10). The reduced chi-squared values are shown in Figure A7. The exposure corrected flux maps are shown in Figure A8.

### 2.3.4 G11.2-0.3

The significant thermal emission from the SNR shell fills the remnant and dominates the low energy band with a significant line apparent near 3 keV (Figure 11). We therefore filter the input image and spectral fitting range to 3.5 – 8 keV to filter out the non-thermal emission from the PWN (Figure 12). The spectral maps appear to show changes with time (Figure 13), however all of the differences are well within the error limits. This is likely due to the relative brevity of the 2000 and 2003 observations leading to large error ranges

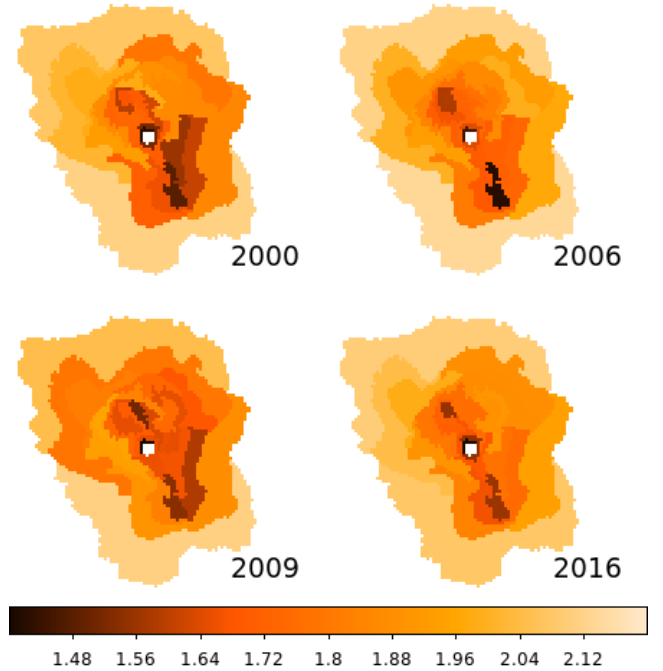


**Figure 6.** Photon index maps vs time for Kes 75. Variability is observed in the jet and surrounding nebula.

in the accompanying spectra (Figure A9). Fitting all observations simultaneously to produce a single spectral map merely reproduces the 2013 map which supports this statement. The reduced chi-squared values are shown in Figure A10. Figure A11 shows the exposure corrected flux maps.

### 2.3.5 3C 58

When fit with a single power-law model, the map of reduced chi-squared (Figure 14) displays regions where the fit is poor near the edge of the PWN indicating the single power-law model is inadequate. We add a VPSHOCK model to describe the thermal emission which drastically improves the fit. Comparing the spectral maps from 2000 and 2003 (Figure 15) paired with the significance image (Figure 16) we find several regions surrounding the pulsar which have significantly hardened over this period. The component error and reduced chi-squared maps with the added two component model regions are shown in Figures A12 and A13. Figure A14 shows the exposure corrected flux maps.

## 3 ALTERNATIVE BINNING METHODS

A previous examination of adaptively binned spectral maps was presented in Kargaltsev et al. (2017). Using a weighted Voronoi tessellations (WVT) method they analyze among others the sample of remnants we have studied here. While they simultaneously fit all available observations of each target, their analysis provides an opportunity to contrast the different binning methods. The regions generated by the WVT method do not follow the surface brightness for thin or elongated features such as the southern jet in Kes 75 unless

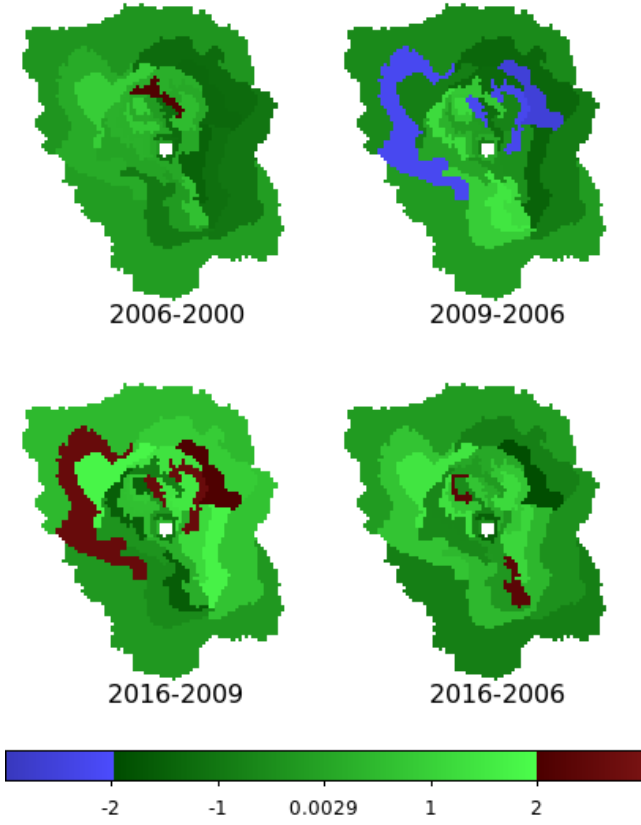


**Figure 7.** Significance maps of Kes 75. Positive (negative) values correspond to softened (hardened) photon index. The southern jet is visible as a region of softened emission along with a region to the north of the counter jet.

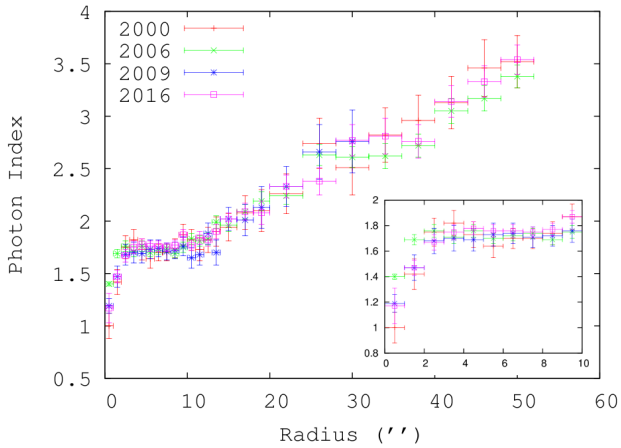


**Figure 8.** Kes 75 radial spectral profile. The radially averaged spectral index does not change significantly with time over 16 years of observations. The softening of the pulsar emission post outburst is visible however there are no long lasting effects in the nebula. The 2009 profile extends only to 30'' due to the position on the ACIS detector.

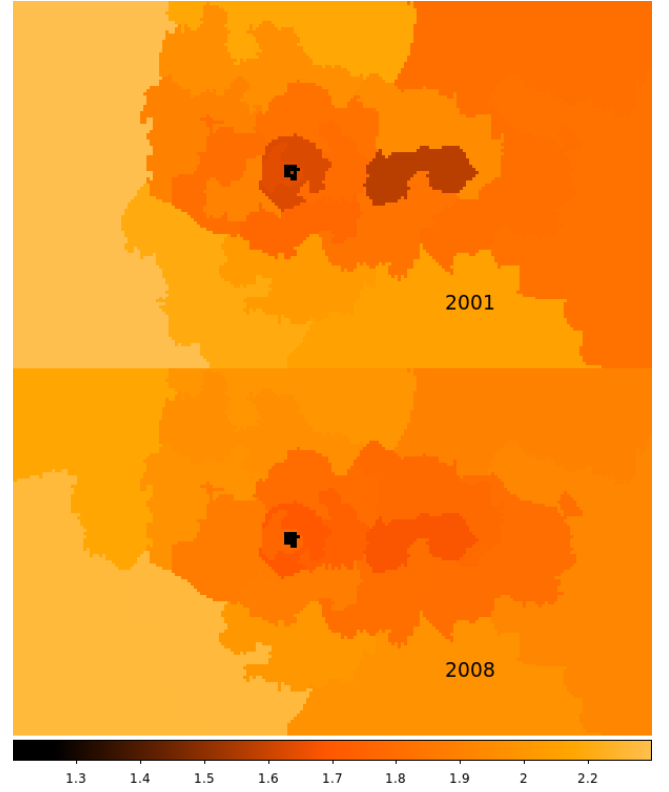


**Figure 9.** G54.1+0.3 spectral maps. While there appears to be some evidence of softening in the torus and western jet the difference is not considered significant (Figure 10).

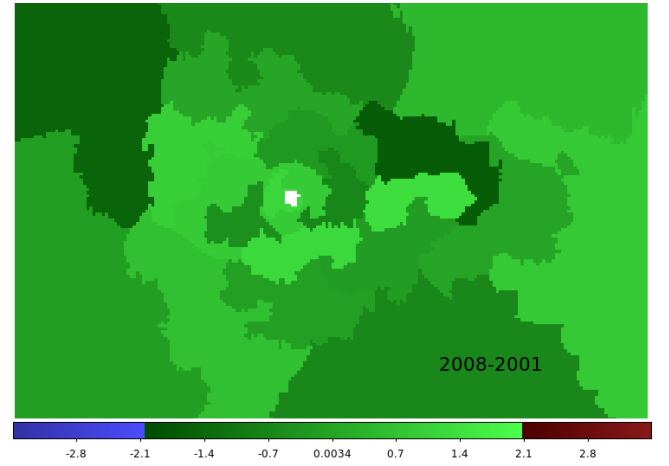


**Figure 10.** G54.1+0.3 Significance map. We find no significant differences and attribute this to the large errors associated with the brief 2001 observation.

the brightness coupled with the length of observation allows for the regions to be smaller than the observed features. For fainter targets with thin features the WVT method does not utilize the imaging resolution of *Chandra*, as the generated regions effectively smooth these features into their surroundings. For the case of Kes 75 this results in an artificial soft-

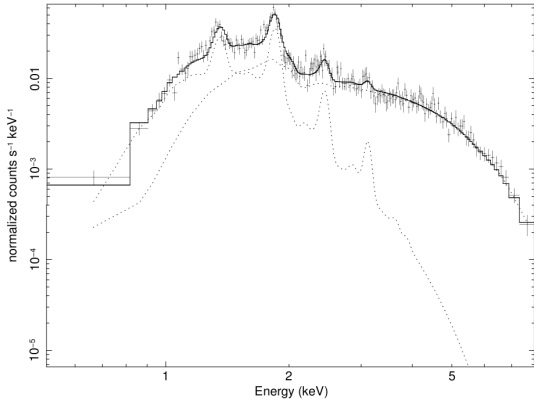


**Figure 11.** G11.2-0.3 sample spectrum of one of the selected regions displayed with the best fit (solid line) thermal (VPSHOCK) plus non-thermal (Power-law) model. The dotted line shows the components of the model spectrum fitted to the data.

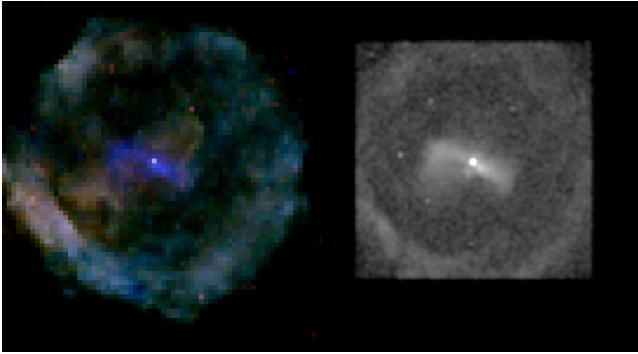


**Figure 12.** Left: RGB *Chandra* Image of G11.2-0.3 with colours defined as 0.5-1.2 keV: red, 1.2-2 keV: green, and 2-7 keV: blue. Right: Filtered 3.5-8 keV image used for spectral map region generation.

ening of the southern jet. Our spectral map of Kes 75 shows the jet feature in isolation from its surroundings.

#### 4 CONCLUSIONS

Spectral maps are a powerful tool which has been under-utilised by the X-ray observing community to study the physics of pulsar wind propagation. We find evidence of variability in G21.5-0.9 in the form of hardening and softening of features resembling an outflow from the pulsar, hardening of the region surrounding the pulsar in 3C 58, hardening of the jets post outburst in Kes 75 followed by softening to return to the pre-outburst state. We find marginal evidence of variability in G11.2-0.3 and G54.1+0.3 which require longer observations to confirm. Examining effects such as the contamination build up on the ACIS detector, we find that this should introduce a systematic hardening which can not explain our observations which show both hardening and

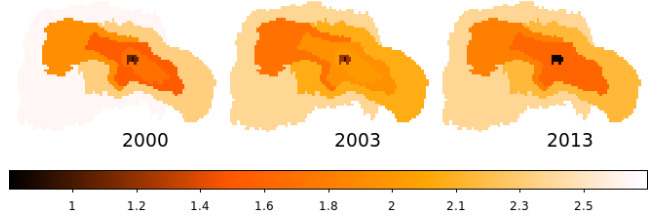


**Figure 13.** Maps of the photon index values in the PWN of G11.2-0.3

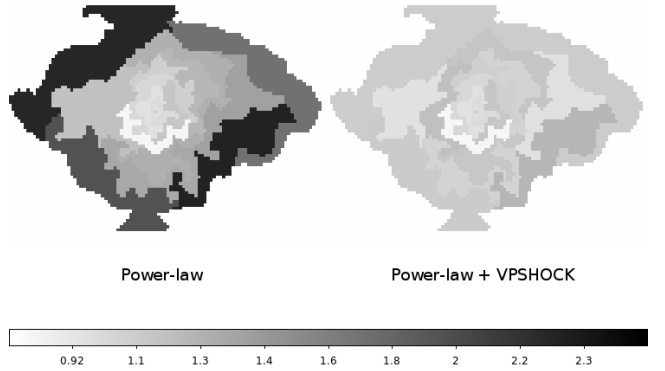


**Figure 14.** 3C 58: Maps of the reduced chi-squared value using an absorbed power-law model (left) and adding a vps shock model where required (right).

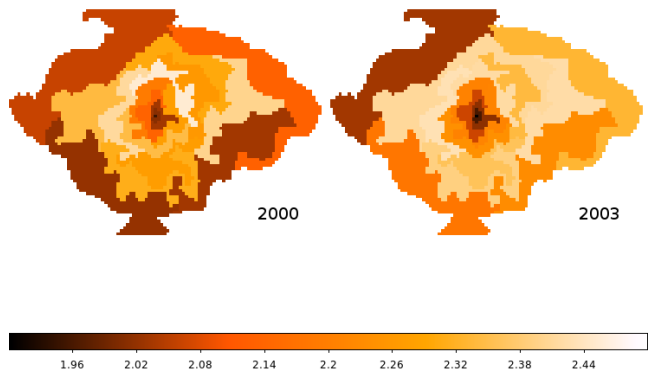


**Figure 15.** Photon index map of 3C 58. The maps are coloured by photon index with darker colours indicating a harder spectrum.

softening. We see differences at a  $2\sigma$  level using the existing archived observations; more and deeper observations of these and other pulsar wind nebulae are needed to enlarge the sample and improve the statistics to meet the standard  $3\sigma$  level. However it is worth noting that we find similari-



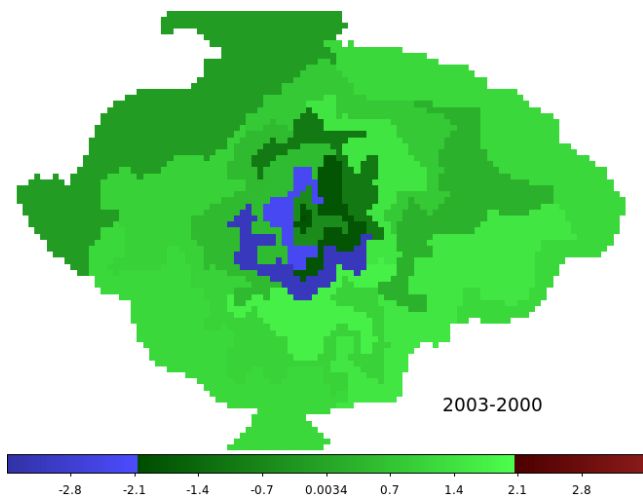


**Figure 16.** Significance map of 3C 58 comparing the 2000 to 2003 observations. Positive (negative) values correspond to softened (hardened) photon index between observations. The region surrounding the central pulsar and jet/torus structure has hardened between the observations.

ties between previous imaging variability studies and some regions that show variability from our spectral index maps.

In particular, the plume of variable emission to the north of the pulsar in G21.5–0.9 (Section 2.3.1) appears in the same location as wisp like features seen in brightness images (Matheson & Safi-Harb (2010); Guest et al. (2019)). The jets in Kes 75 where we see changes have been observed to vary in brightness (Reynolds et al. (2018)). As well as future observations, modelling and comparisons with 3D MHD simulations are required to understand the origins of this newly revealed form of variability. This is beyond the scope of this paper and will be the subject of future follow-up work.

## ACKNOWLEDGEMENTS

This research was supported by the Natural Sciences and Engineering Research Council of Canada (NSERC), and made use of the SAO/NASA Astrophysics Data System and the University of Manitoba’s High-Energy Catalogue of Supernova Remnants (SNRcat<sup>1</sup>, Ferrand & Safi-Harb (2012)). We thank Eric V. Gotthelf and Craig Heinke for comments, and an anonymous referee for a detailed review that helped improve this paper.

## REFERENCES

- Arnaud K. A., 1996, in Jacoby G. H., Barnes J., eds, *Astronomical Society of the Pacific Conference Series Vol. 101, Astronomical Data Analysis Software and Systems V*. p. 17
- Bietenholz M. F., Bartel N., 2008, *MNRAS*, **386**, 1411
- Blumer H., Safi-Harb S., McLaughlin M. A., 2017, *ApJ*, **850**, L18
- Bocchino F., van der Swaluw E., Chevalier R., Bandiera R., 2005, *A&A*, **442**, 539

<sup>1</sup> <http://snrcat.physics.umanitoba.ca/>

- Borkowski K. J., Reynolds S. P., Roberts M. S. E., 2016, *ApJ*, **819**, 160
- Camilo F., Lorimer D. R., Bhat N. D. R., Gotthelf E. V., Halpern J. P., Wang Q. D., Lu F. J., Mirabal N., 2002, *ApJ*, **574**, L71
- Camilo F., Ransom S. M., Gaensler B. M., Slane P. O., Lorimer D. R., Reynolds J., Manchester R. N., Murray S. S., 2006, *ApJ*, **637**, 456
- DeLaney T., Gaensler B. M., Arons J., Pivovarov M. J., 2006, *ApJ*, **640**, 929
- Del Zanna L., Pili A. G., Olmi B., Bucciantini N., Amato E., 2018, *Plasma Physics and Controlled Fusion*, **60**, 014027
- Ferrand G., Safi-Harb S., 2012, *Advances in Space Research*, **49**, 1313
- Fruscione A., et al., 2006, CIAO: Chandra’s data analysis system. SPIE, p. 62701V, doi:10.1117/12.671760
- Gavril F. P., Gonzalez M. E., Gotthelf E. V., Kaspi V. M., Livingstone M. A., Woods P. M., 2008, *Science*, **319**, 1802
- Gotthelf E. V., Vasisht G., Boylan-Kolchin M., Torii K., 2000, *ApJ*, **542**, L37
- Gotthelf E. V., Helfand D. J., Newburgh L., 2007, *ApJ*, **654**, 267
- Guest B. T., Safi-Harb S., Tang X., 2019, *MNRAS*, **482**, 1031
- Gupta Y., Mitra D., Green D. A., Acharyya A., 2005, *Current Science*, **89**, 853
- Helfand D. J., Collins B. F., Gotthelf E. V., 2003, *ApJ*, **582**, 783
- Hester J. J., et al., 2002, *ApJ*, **577**, L49
- Kargaltsev O., Klingler N., Chastain S., Pavlov G. G., 2017, in *Journal of Physics Conference Series*. p. 012050 (arXiv:1711.02656), doi:10.1088/1742-6596/932/1/012050
- Kaspi V. M., Roberts M. E., Vasisht G., Gotthelf E. V., Pivovarov M., Kawai N., 2001, *ApJ*, **560**, 371
- Kennel C. F., Coroniti F. V., 1984a, *ApJ*, **283**, 694
- Kennel C. F., Coroniti F. V., 1984b, *ApJ*, **283**, 710
- Kothes R., 2013, *A&A*, **560**, A18
- Kothes R., 2016, in *Supernova Remnants: An Odyssey in Space after Stellar Death*. p. 46
- Kumar H. S., Safi-Harb S., 2008, *ApJ*, **678**, L43
- Lu F. J., Wang Q. D., Aschenbach B., Durouchoux P., Song L. M., 2002, *ApJ*, **568**, L49
- Matheson H., Safi-Harb S., 2005, *Advances in Space Research*, **35**, 1099
- Matheson H., Safi-Harb S., 2010, *ApJ*, **724**, 572
- Minter A. H., Camilo F., Ransom S. M., Halpern J. P., Zimmerman N., 2008, *ApJ*, **676**, 1189
- Morton T. D., Slane P., Borkowski K. J., Reynolds S. P., Helfand D. J., Gaensler B. M., Hughes J. P., 2007, *ApJ*, **667**, 219
- Murray S. S., Slane P. O., Seward F. D., Ransom S. M., Gaensler B. M., 2002, *ApJ*, **568**, 226
- Ng C.-Y., Slane P. O., Gaensler B. M., Hughes J. P., 2008, *ApJ*, **686**, 508
- Pavlov G. G., Kargaltsev O. Y., Sanwal D., Garmire G. P., 2001, *ApJ*, **554**, L189
- Porth O., Vorster M. J., Lyutikov M., Engelbrecht N. E., 2016, *MNRAS*, **460**, 4135
- Reynolds S. P., Borkowski K. J., Gwynne P. H., 2018, *ApJ*, **856**, 133
- Roberts M. S. E., Tam C. R., Kaspi V. M., Lyutikov M., Vasisht G., Pivovarov M., Gotthelf E. V., Kawai N., 2003, *ApJ*, **588**, 992
- Safi-Harb S., Harrus I. M., Petre R., Pavlov G. G., Koptsevich A. B., Sanwal D., 2001, *ApJ*, **561**, 308
- Sanders J. S., 2006, *MNRAS*, **371**, 829
- Shan S. S., Zhu H., Tian W. W., Zhang M. F., Zhang H. Y., Wu D., Yang A. Y., 2018, *ApJS*, **238**, 35
- Slane P., Chen Y., Schulz N. S., Seward F. D., Hughes J. P., Gaensler B. M., 2000, *ApJ*, **533**, L29
- Slane P., Helfand D. J., van der Swaluw E., Murray S. S., 2004, *ApJ*, **616**, 403
- Stephenson F. R., 1971, *QJRAS*, **12**, 10

- Tang X., Chevalier R. A., 2012, [ApJ](#), **752**, 83  
 Temim T., Slane P., Reynolds S. P., Raymond J. C., Borkowski  
 K. J., 2010, [ApJ](#), **710**, 309  
 Tian W. W., Leahy D. A., 2008, [MNRAS](#), **391**, L54  
 Torii K., Tsunemi H., Dotani T., Mitsuda K., 1997, [ApJ](#), **489**,  
 L145  
 Vasisht G., Aoki T., Dotani T., Kulkarni S. R., Nagase F., 1996,  
[ApJ](#), **456**, L59  
 Verbiest J. P. W., Weisberg J. M., Chael A. A., Lee K. J., Lorimer  
 D. R., 2012, [ApJ](#), **755**, 39  
 Wilms J., Allen A., McCray R., 2000, [ApJ](#), **542**, 914  
 Younes G., et al., 2016, [ApJ](#), **824**, 138

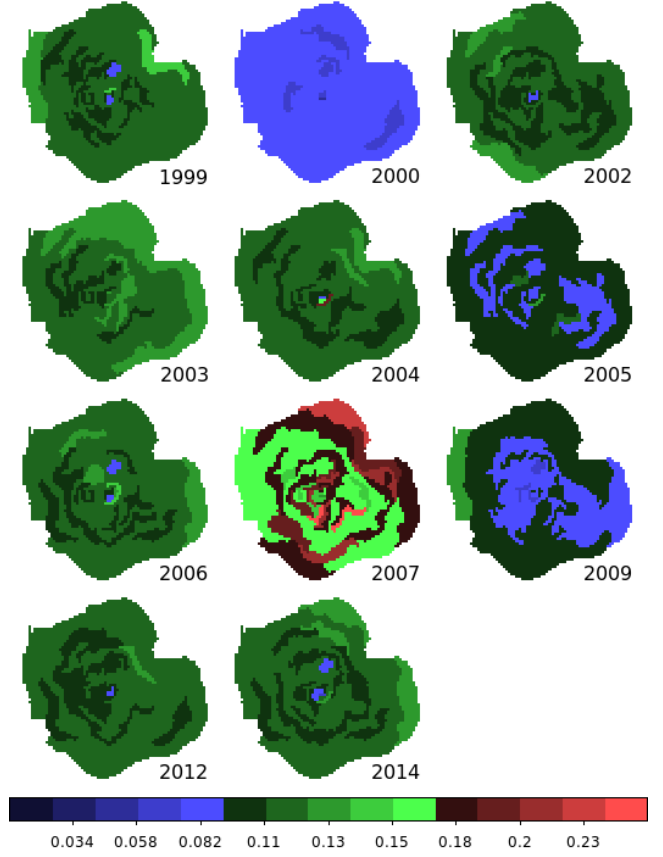


**Figure A1.**  $1 - \sigma$  error values of the photon index associated with the fits to G11.2-0.3 shown in Figure 2.

## APPENDIX A: ADDITIONAL PARAMETER MAPS

This paper has been typeset from a  $\text{\LaTeX}$  file prepared by the author.

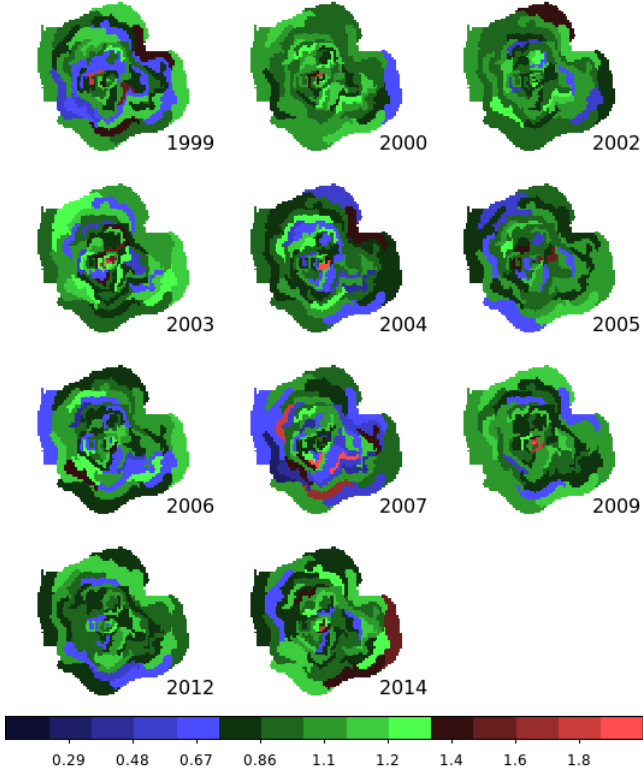


**Figure A2.** Reduced chi-squared values associated with the fits to G11.2-0.3 shown in Figure 2.

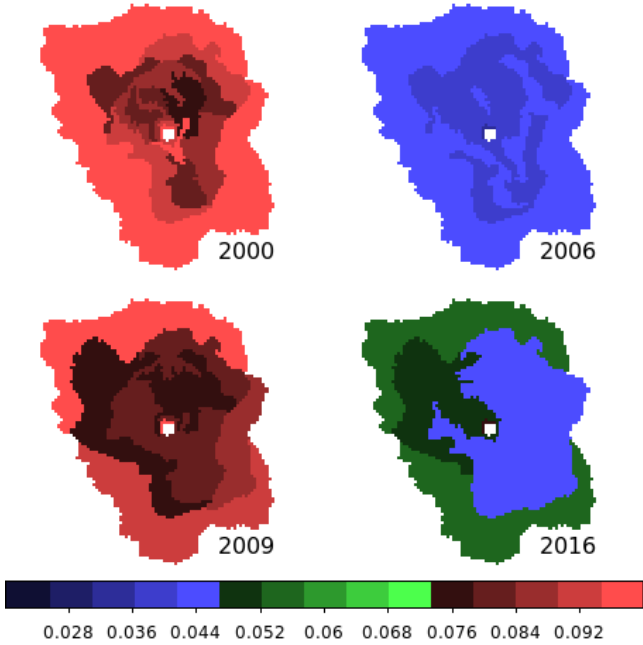


**Figure A3.**  $1 - \sigma$  error values in the photon index associated with the fits to Kes 75 shown in Figure 6.

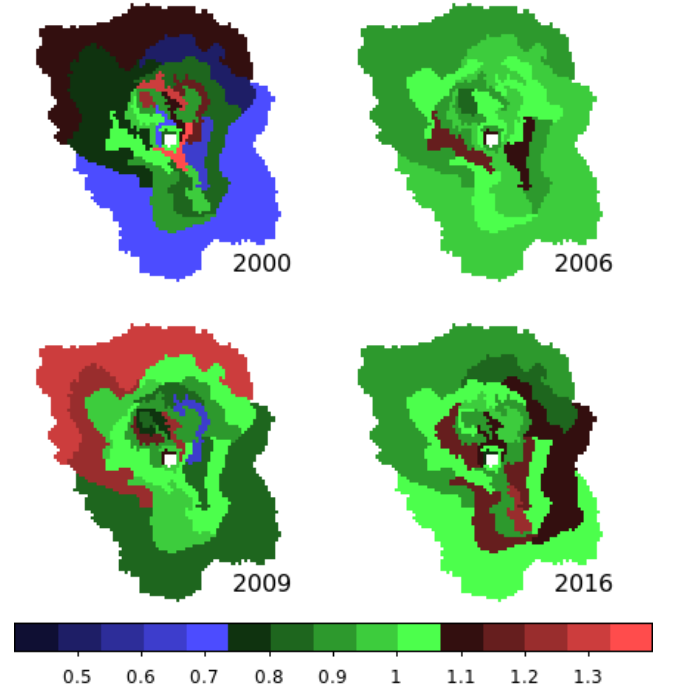


**Figure A4.** Reduced chi-squared values of the fits to Kes 75 shown in Figure 6.

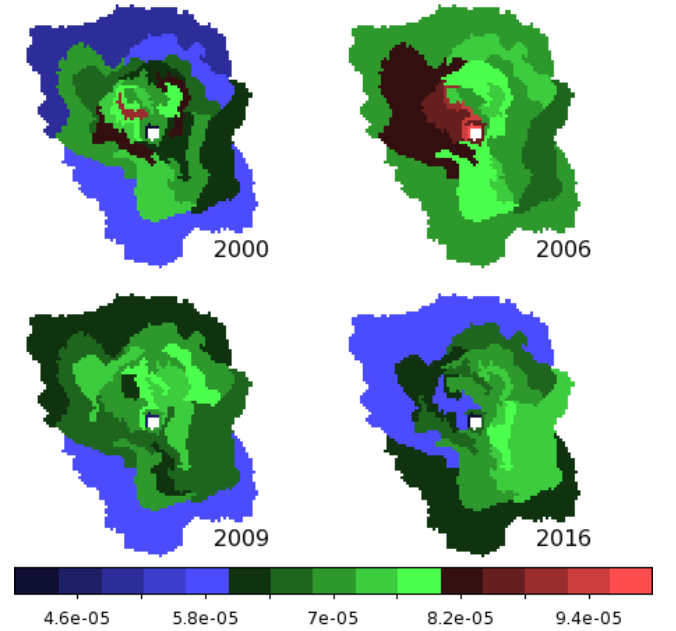


**Figure A5.** Exposure corrected flux maps of Kes 75 (in units of photons  $\text{cm}^{-2}\text{s}^{-1}$ ).

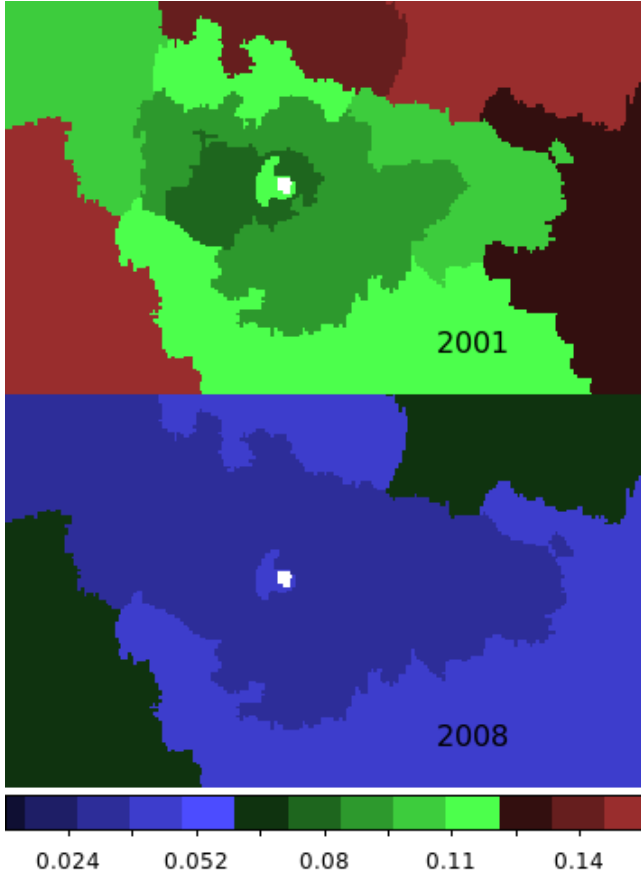


**Figure A6.**  $1-\sigma$  errors of the photon index associated with the fits to G54.1+0.3 shown in Figure 9.

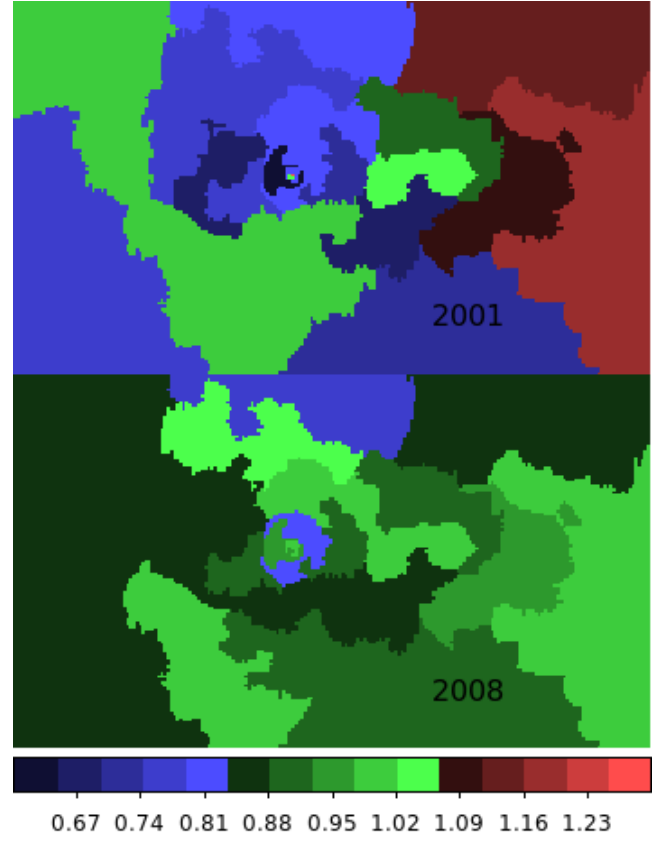


**Figure A7.** Reduced chi-squared values of the fits to G54.1+0.3 shown in Figure 9.

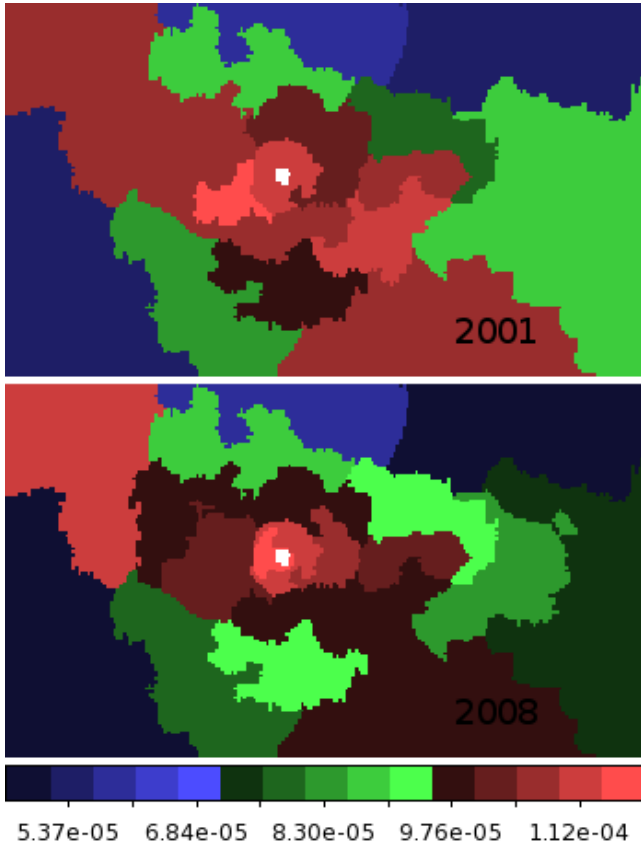


**Figure A8.** Exposure corrected flux maps of G54.1+0.3 (in units of photons  $\text{cm}^{-2}\text{s}^{-1}$ ).

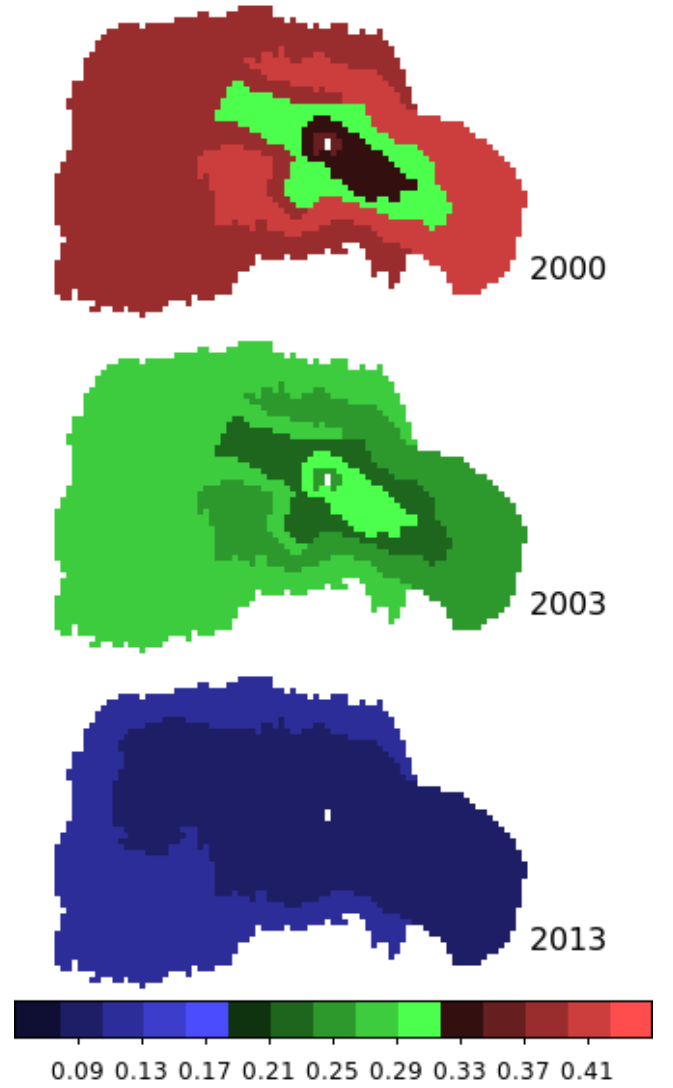


**Figure A9.**  $1 - \sigma$  error values of the photon index associated with the fits to G11.2-0.3 shown in Figure 13.



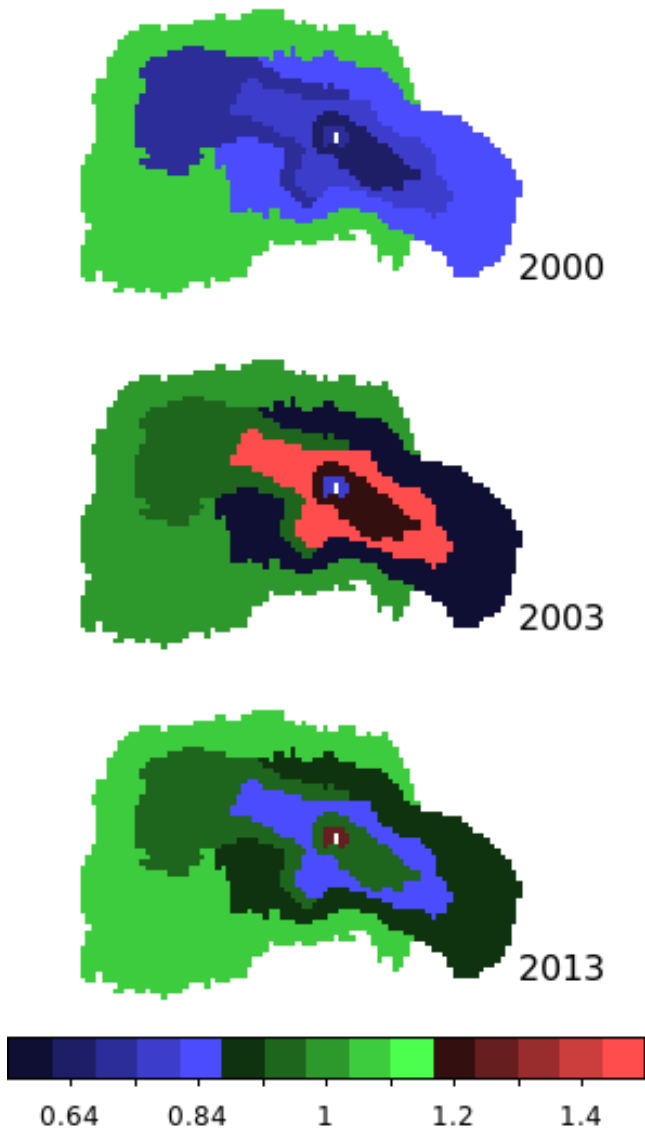


**Figure A10.** Reduced chi-squared values of the fits to G11.2-0.3 shown in Figure 13.

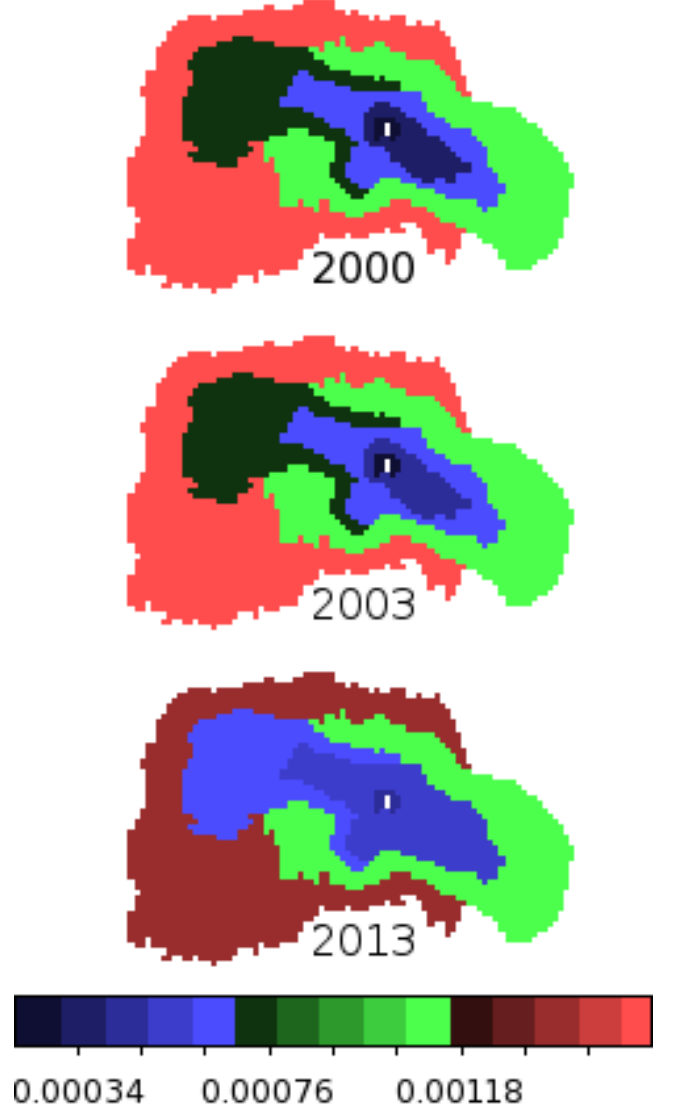


**Figure A11.** Exposure corrected flux maps of G11.2-0.3 (in units of photons  $\text{cm}^{-2}\text{s}^{-1}$ ).

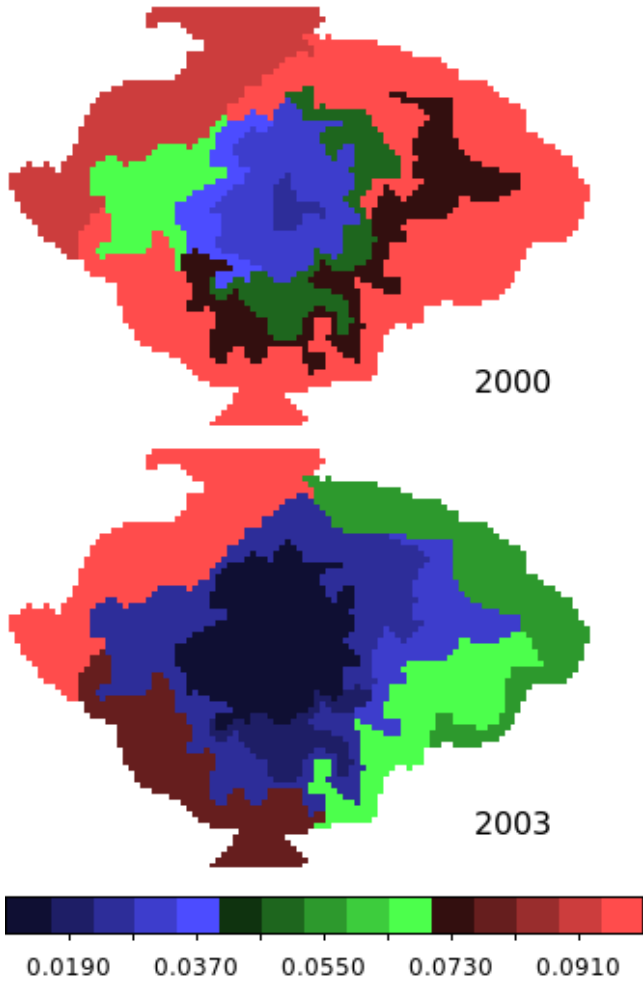


**Figure A12.**  $1 - \sigma$  error values of the photon index associated with the fits to 3C58 shown in Figure 15.

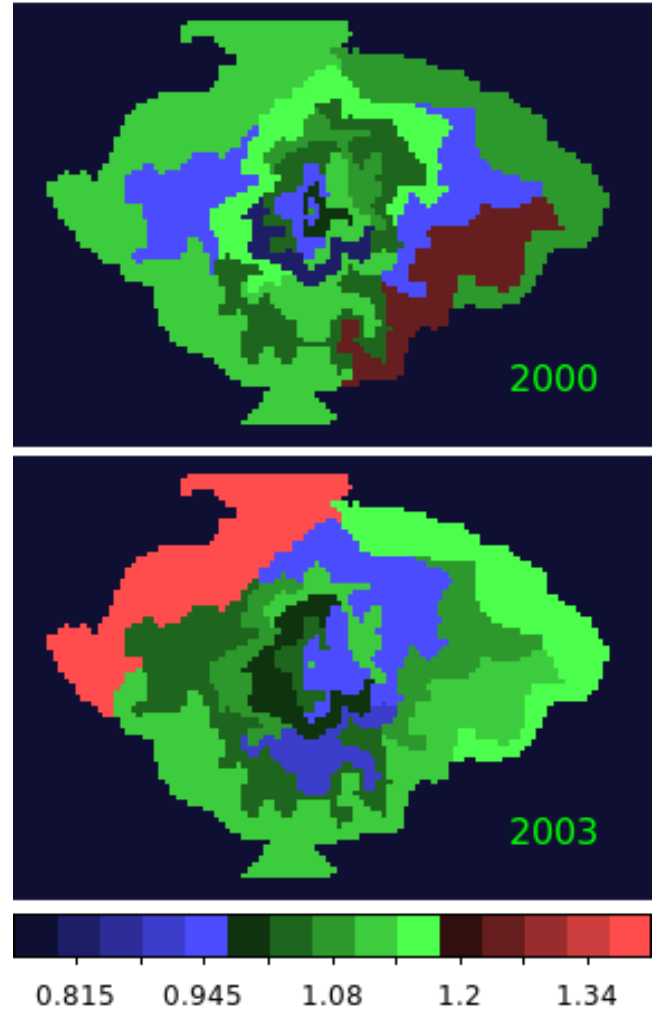


**Figure A13.** Reduced chi-squared values of the fits to 3C58 shown in Figure 15.

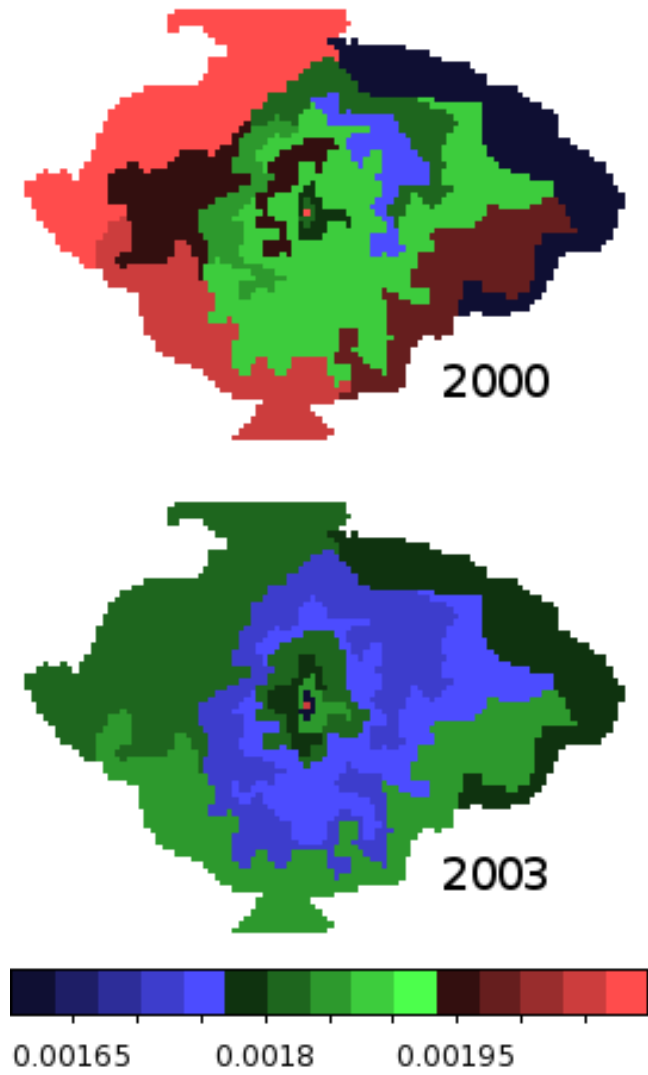


**Figure A14.** Exposure corrected flux maps of 3C58 (in units of photons  $\text{cm}^{-2}\text{s}^{-1}$ ).